JOM, Vol. 67, No. 11, 2015
DOI: 10.1007/s11837-015-1617-z

Design of Refractory High-Entropy Alloys

M.C. GAO,[1,2,3] C.S. CARNEY,[1,2] Ö.N. DOĞAN,[1] P.D. JABLONKSI,[1] J.A. HAWK,[1] and D.E. ALMAN[1]

1.—National Energy Technology Laboratory, Albany, OR 97321, USA. 2.—AECOM, Albany, OR 97321, USA. 3.—e-mail: michael.gao@netl.doe.gov

This report presents a design methodology for refractory high-entropy alloys with a body-centered cubic (bcc) structure using select empirical parameters (i.e., enthalpy of mixing, atomic size difference, Ω-parameter, and electronegativity difference) and CALPHAD approach. Sixteen alloys in equimolar compositions ranging from quinary to ennead systems were designed with experimental verification studies performed on two alloys using x-ray diffraction, energy-dispersive spectroscopy, and scanning electron microscopy. Two bcc phases were identified in the as-cast HfMoNbTaTiVZr, whereas multiple phases formed in the as-cast HfMoNbTaTiVWZr. Observed elemental segregation in the alloys qualitatively agrees with CALPHAD prediction. Comparisons of the thermodynamic mixing properties for liquid and bcc phases using the Miedema model and CALPHAD are presented. This study demonstrates that CALPHAD is more effective in predicting HEA formation than empirical parameters, and new single bcc HEAs are suggested: HfMoNbTiZr, HfMoTaTiZr, NbTaTiVZr, HfMoNbTaTiZr, HfMoTaTiVZr, and MoNbTaTiVZr.

INTRODUCTION

Multicomponent solid-solution alloys were proposed independently by Yeh et al.[1] as high-entropy alloys (HEAs) and by Cantor et al.[2] as equiatomic multicomponent alloys in 2004. Yeh[3] provided two definitions for HEAs. One is based on chemical composition, in which HEAs are defined to preferentially contain at least five principal elements, each with an atomic percentage between 5% and 35%. The other is based on configurational entropy, in which HEAs are defined as alloys having configurational entropies at a random state ≥1.5R (R is the ideal gas constant), no matter whether they are single phase or multiphase at room temperature. References [4] and [5] provide comprehensive reviews on the formation, microstructures, and properties of HEAs.

Empirical rules for formation of HEAs are addressed from the considerations of enthalpy of mixing (ΔH_{mix}),[6] atomic size difference (δ),[6] Ω-parameter,[7,8] and electronegativity difference ($\Delta\chi$).[9] The HEA crystal structure is addressed from the valence electron concentration (VEC).[10] Although these guidelines are useful, the number of single-phase HEAs is still very limited. Gao and Alman[11] proposed an effective searching strategy by combining experimental phase diagram inspection, CALPHAD (acronym of calculation of phase diagram) modeling, and ab initio molecular dynamics (AIMD) simulations, and they suggested new single face-centered cubic (fcc) and hexagonal close-packed (hcp) HEAs. Accelerating the HEA design using the CALPHAD approach has been addressed by Zhang et al.,[12–14] Gao et al.,[15,16] and Senkov et al.[17] Very recently Troparevsky et al.[18] proposed a searching scheme based on enthalpy data of binary compounds calculated from first-principles density functional theory (DFT) and suggested a series of new single-phase HEAs. The main objective of the current study was to design single-phase refractory HEAs with the body centered cubic (bcc) structure that contains five or more components in equimolar composition. The other objective was to compare and contrast the effectiveness of using empirical parameters versus the CALPHAD approach.

(Published online September 15, 2015)

Table I. Calculated empirical and thermodynamic parameters

#	Alloy composition	T_m (K) average	T_{liq} (K) CAL	ρ g/cm^3	δ (%)	$\Delta\chi$	ΔS_{mix} (J/K/mol)			ΔH_{mix} (kJ/mol)			Ω		
										Liquid			Liquid		
							Ideal	Liquid CAL	BCC CAL	Tak[19]	CAL[a]	BCC CAL[b]	Tak[19]	CAL[a]	BCC CAL[b]
1	HfMoNbTiZr	2444	2184	8.70	5.06	0.40	13.38	13.14	12.70	−1.6	−3.1	0.4	20.4	9.3	66.1
2	HfMoTaTiZr	2552	2317	10.21	5.06	0.38	13.38	13.26	12.50	−1.9	−2.4	0.7	17.8	12.9	41.4
3	MoNbTaTiZr[7]	2601	2480	9.14	4.42	0.31	13.38	12.85	12.33	−1.8	−2.5	0.3	19.8	12.5	108.4
4	NbTaTiVZr	2458	2202	8.50	5.39	0.38	13.38	13.17	12.50	0.3	0.8	4.3	102.8	35.1	6.4
5	CrMoNbTaVW[27]	2832	2813	11.68	4.78	0.32	14.90	13.86	14.68	−4.9	−5.4	−0.7	8.6	7.2	62.3
6	HfMoNbTaTiZr	2586	2389	9.95	4.70	0.34	14.90	14.73	14.11	−0.9	−2.0	0.9	43.3	17.4	36.9
7	HfNbTaTiVZr[15]	2466	2151	9.44	5.59	0.41	14.90	14.94	14.59	0.8	0.8	5.1	47.2	39.7	6.2
8	HfMoTaTiVZr	2491	2299	9.70	6.07	0.42	14.90	14.66	14.10	−3.2	−1.5	2.1	11.5	22.1	15.6
9	MoNbTaTiVW[14]	2793	2826	10.97	3.10	0.33	14.90	14.01	13.39	−4.2	−3.7	−3.4	9.9	10.7	11.2
10	MoNbTaTiVZr	2532	2438	8.75	5.27	0.34	14.90	14.38	13.87	−2.1	−1.5	1.3	17.9	23.9	26.3
11	HfMoNbTaTiVZr	2528	2345	9.54	5.62	0.26	16.18	15.94	15.46	−1.5	−1.4	2.0	27.8	26.3	17.9
12	HfMoNbTaTiVWZr	2674	2531	10.25	5.49	0.36	17.29	16.39	16.05	−2.9	−3.3	1.3	15.7	12.6	30.8
13	CrHfMoNbTaTiVWZr	2619	2443	9.86	4.95	0.33	18.27	17.34	17.66	−2.9	−3.6	3.4	16.7	11.6	12.8
14	MoNbTaW[25]	3158	3137	13.63	2.27	0.36	11.53	10.74	10.04	−6.5	−7.5	−8.7	5.6	4.5	3.6
15	MoNbTaVW[25]	2963	2977	10.97	3.21	0.34	13.38	12.18	11.66	−4.6	−6.2	−6.6	8.5	5.8	5.3
16	HfNbTaTiZr[26]	2523	2279	8.63	4.01	0.12	13.38	13.67	13.22	2.7	1.8	4.7	12.5	17.7	6.4

CAL refers to CALPHAD, and Tak refers to data taken from Takeuchi et al.[19] via Eq. 1.[a]The reference states of all components were the liquid phase at 1 atm.[b]The reference states of all components were the bcc phase at 1 atm.

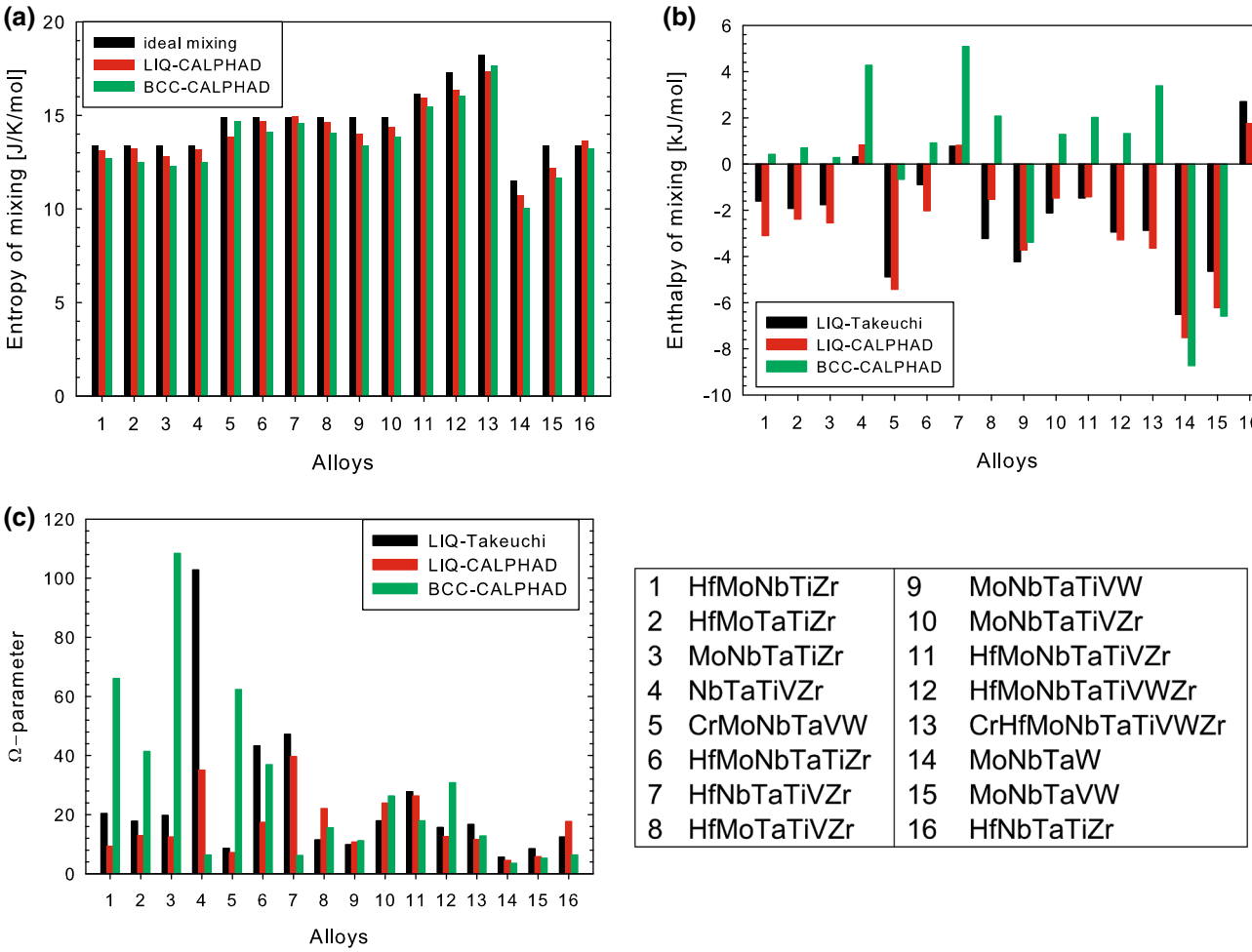

Fig. 1. Comparison in (a) entropy of mixing, (b) enthalpy of mixing, and (c) Ω-parameter for the liquid and bcc phases.

COMPUTER MODELING METHODOLOGIES

Empirical Parameters

The calculated empirical parameters are listed in Table I, with the equations used in their development presented in this subsection. The enthalpy of mixing for an alloy is calculated by:

$$\Delta H_{\text{mix}} = 4 \sum_{i=1, i\neq j}^{N} \Delta H_{ij}^{\text{mix}} x_i x_j, \tag{1}$$

where x_i (x_j) is the composition of the ith (jth) element, $\Delta H_{ij}^{\text{mix}}$ is the enthalpy of mixing between element i and j in the liquid state at equimolar compositions taken from the table edited by Takeuchi et al.,[19] which was based on the Miedema model,[20] and N is the total number of elements in the solution phase. For a comparison, the ΔH_{mix} values for the bcc and liquid phases are also calculated using CALPHAD in this study.

The atomic size difference measures composition-weighted difference in the atomic radii among constituent elements and is calculated by:

$$\delta = \sqrt{\sum_{i=1}^{N} x_i \left(1 - x_i / \sum_{j=1}^{N} x_j r_j\right)^2}, \tag{2}$$

where $r_i(r_j)$ is the atomic radius of the ith (jth) element.

The HEA community has approximated the total entropy of mixing (ΔS_{mix}) of an HEA in the solid state by the ideal configurational entropy ($\Delta S_{\text{mix}}^{\text{conf}}$) and is calculated by:

$$\Delta S_{\text{mix}}^{\text{conf}} = -R \sum_{i=1}^{N} x_i \ln x_i, \tag{3}$$

The Ω parameter correlates the melting point, total entropy of mixing, and the total enthalpy of mixing (ΔH_{mix}) as:

$$\Omega = \frac{T_{\text{m}} \Delta S_{\text{mix}}}{|\Delta H_{\text{mix}}|}, \tag{4}$$

where T_{m} is the average melting temperature of the alloy (i.e., $T_{\text{m}} = \sum_i x_i T_{\text{m}}^i$, where T_{m}^i is the melting point of component i), and ΔS_{mix} and ΔH_{mix} are the

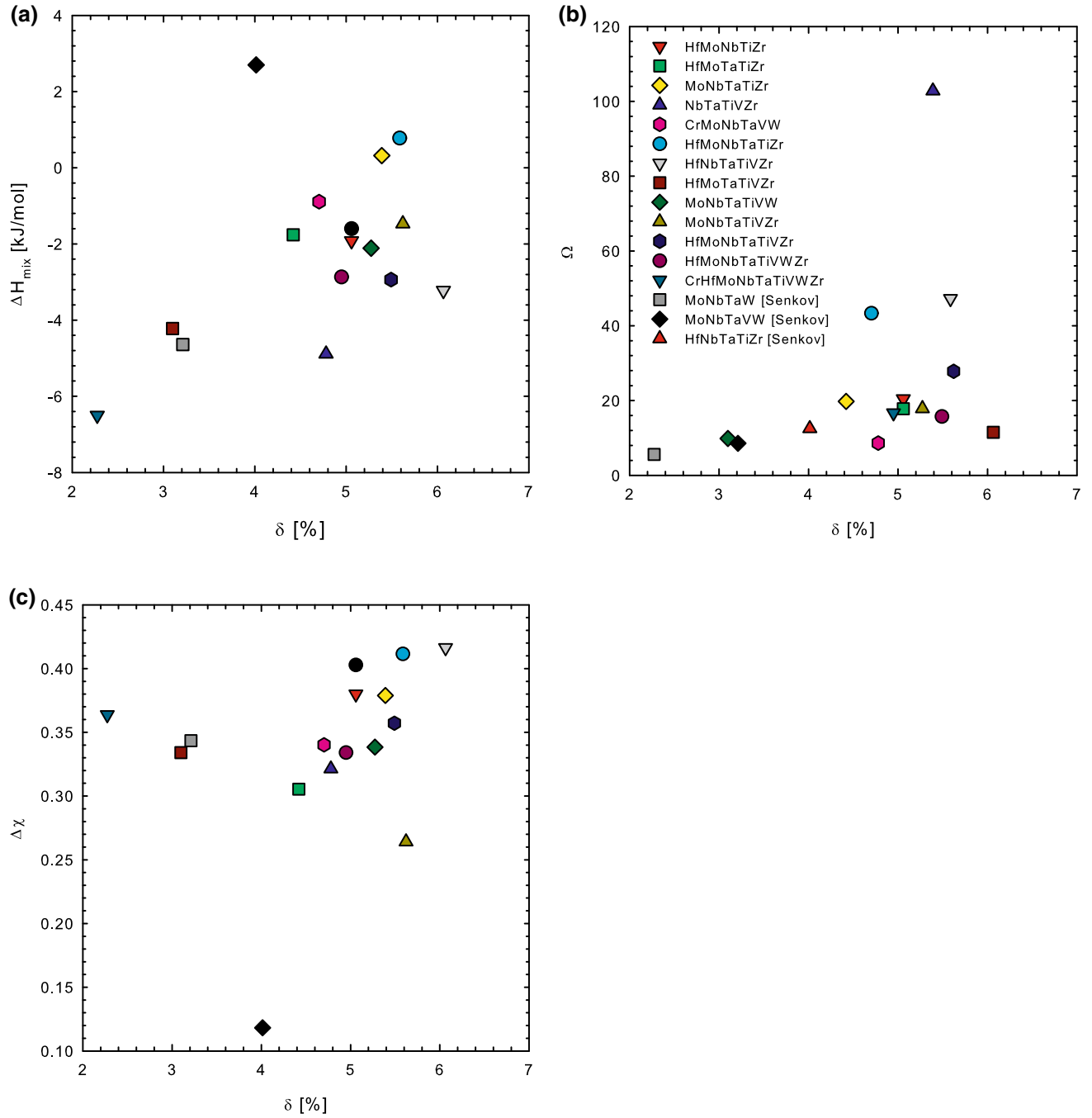

Fig. 2. Calculated empirical parameters: (a) ΔH_{mix}^{liq} from Miedema model, (b) Ω, and (c) $\Delta\chi$ with respect to δ.

total entropy of mixing and enthalpy of mixing of the liquid phase, respectively. However, generally speaking, both ΔS_{mix} and ΔH_{mix} for the solid-solution phases should vary depending on their crystal structures, and they may not be available from empirical models. These values for the bcc phase and the liquidus temperature (T_{liq}) are calculated using CALPHAD method in this study.

The electronegativity difference in a multicomponent system was previously proposed by Fang et al.[21] for bulk metallic glasses (BMGs):

$$\Delta\chi = \sqrt{\sum_{i=1}^{N} x_i \left(\chi_i - \sum_{j=1}^{N} x_j \chi_j\right)^2}, \qquad (5)$$

where χ_i (χ_j) is the Pauling electronegativity of the ith (jth) element.

The density of the alloy was estimated using the rule of mixture:

$$\rho_{mix} = \frac{\sum_{i=1}^{N} x_i W_i}{\sum_{i=1}^{N} x_i W_i / \rho_i}, \qquad (6)$$

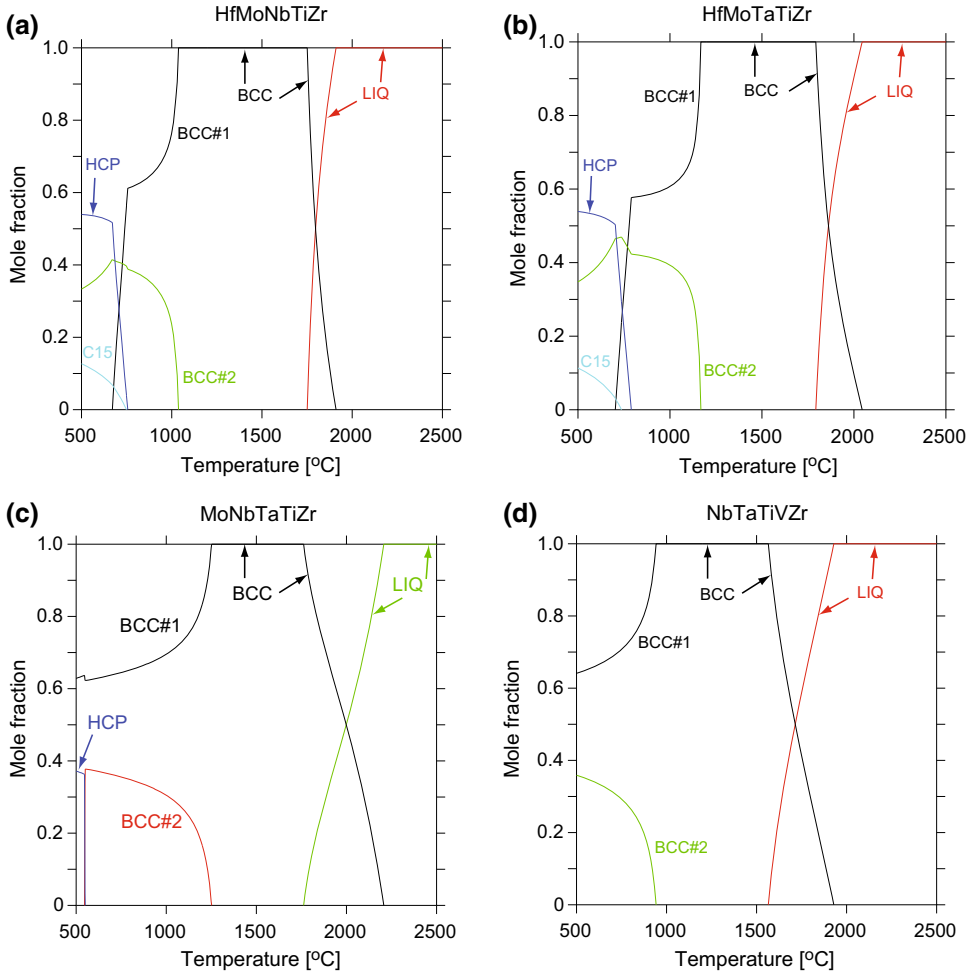

Fig. 3. Calculated equilibrium mole fraction for quinary HEAs: (a) HfMoNbTiZr, (b) HfMoTaTiZr, (c) MoNbTaTiZr, and (d) NbTaTiVZr.

where x_i, W_i, and ρ_i are the molar composition, atomic weight, and density of each element i, respectively.

CALPHAD Modeling

All CALPHAD calculations were performed using the Thermo-Calc—supplied TCNI7 thermodynamic database (Thermo-Calc Software, McMurray, PA).[22] The nonequilibrium solidification simulation was accomplished using the Scheil–Gulliver models.[23,24]

The total entropy of mixing (ΔS_{mix}), enthalpy of mixing (ΔH_{mix}) and Gibbs energy of mixing (ΔG_{mix}) for bcc and liquid phases were calculated as a function of composition and temperature by:

$$\Delta S^{\varphi}_{\text{mix}} = S^{\varphi}_{\text{m}} - \sum_i x_i S^{\varphi}_i, \tag{7}$$

$$\Delta H^{\varphi}_{\text{mix}} = H^{\varphi}_{\text{m}} - \sum_i x_i H^{\varphi}_i, \tag{8}$$

$$\Delta G^{\varphi}_{\text{mix}} = \Delta H^{\varphi}_{\text{m}} - T\Delta S^{\varphi}_{\text{m}}, \tag{9}$$

where φ refers to the bcc or liquid phase, H^{φ}_{m} (S^{φ}_{m}) is the total enthalpy (entropy) of the φ phase, and H^{φ}_i (S^{φ}_i) is enthalpy (entropy) of component i in the φ structure.

The excess entropy describes the difference between the total entropy and the ideal configurational entropy, namely:

$$^{\text{ex}}S^{\varphi}_{\text{m}} = S^{\varphi}_{\text{m}} + R\sum_i x_i \ln x_i, \tag{10}$$

where R is the ideal gas constant.

MODELING RESULTS

Empirical Parameters

Table I lists the empirical parameters, estimated densities, and thermodynamic properties for the 16 alloys investigated herein. Alloy MoNbTaW,[25] MoNbTaVW,[25] and HfNbTaTiZr[26] are included for comparison purpose. The averaged T_{m} is higher than T_{liq} for most alloys, and the difference is as high as 315°C for HfNbTaTiVZr, except that the

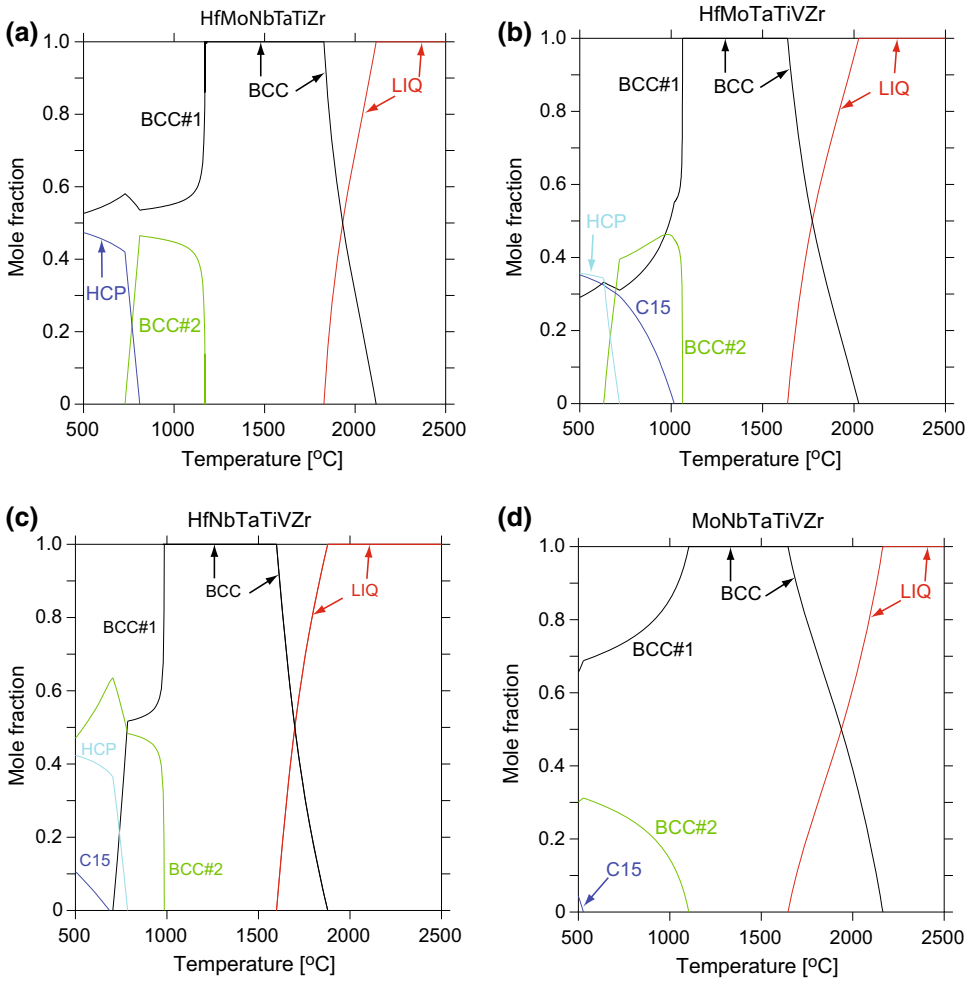

Fig. 4. Calculated equilibrium mole fraction for senary HEAs: (a) HfMoNbTaTiZr, (b) HfMoTaTiVZr, (c) HfNbTaTiVZr, and (d) MoNbTaTiVZr.

agreement is very good only for CrMoNbTaVW, MoNbTaTiVW, MoNbTaW, and MoNbTaVW. Intuitively speaking, a lower liquidus temperature than the average temperature implies that alloying stabilizes the liquid phase more than the competing solid phase. The estimated density is the lowest for NbTaTiVZr (8.50 g/cm^3), whereas MoNbTaW has the highest density of 13.63 g/cm^3. Additionally, all alloys have a relatively small δ; it ranges from 2.27% to 6.07%. Except for very small $\Delta\chi$ for 0.12 for HfNbTaTiZr and 0.26 for HfMoNbTaTiVZr, it otherwise varies in a very narrow range of 0.31–0.42 for the rest of these alloys.

Figure 1 compares the entropy of mixing, enthalpy of mixing, and Ω-parameter for both liquid and bcc phases from different data sources, namely the Takeuchi table[19] using the Miedema model and CALPHAD prediction. The calculated ΔS_{mix} values for the liquid and bcc phases are fairly closer to that for the ideal mixing for all alloys (Fig. 1a). This justifies the common practice in the community to use Eq. 3 to approximate the total entropy of mixing for HEAs for this batch of alloys. However, the calculated ΔH_{mix} values vary noticeably depending on alloy compositions and phases. Overall, the agreement in $\Delta H^{\text{liq}}_{\text{mix}}$ is very good using the Takeuchi table[19] and CALPHAD, and they are all negative except NbTaTiVZr, HfNbTaTiVZr, and HfNbTaTiZr for which the hcp metals constitute ≥50 at.%. MoNbTaW has the most negative $\Delta H^{\text{liq}}_{\text{mix}}$ whereas HfNbTaTiZr has the most positive one. As for the bcc phase (Fig. 1b), $\Delta H^{\text{bcc}}_{\text{mix}}$ are all positive except CrMoNbTaVW, MoNbTaTiVW, MoNbTaW, and MoNbTaVW, which consists of all bcc metals. MoNbTaW has the most negative $\Delta H^{\text{bcc}}_{\text{mix}}$, whereas HfNbTaTiVZr has the most positive one. The calculated Ω parameters (Fig. 1c) are all relatively large (e.g., $\Omega \geq 4.5$ if $\Delta H^{\text{liq}}_{\text{mix}}$ is used, and $\Omega \geq 3.6$ if $\Delta H^{\text{bcc}}_{\text{mix}}$ is used). MoNbTaW has the lowest Ω parameter (Fig. 1c) because it has the most negative enthalpy of mixing. Because of the combined differences from ΔH_{mix}, ΔS_{mix}, and T_{m} versus T_{liq}, the Ω parameter shows much more pronounced contrast between liquid and bcc phases for several alloys. To be consistent with literature, Fig. 2 displays how $\Delta H^{\text{liq}}_{\text{mix}}$ (using Eq. 1 and the Takeuchi table[19]), Ω, and $\Delta\chi$ vary with respect to δ for all 16 alloys.

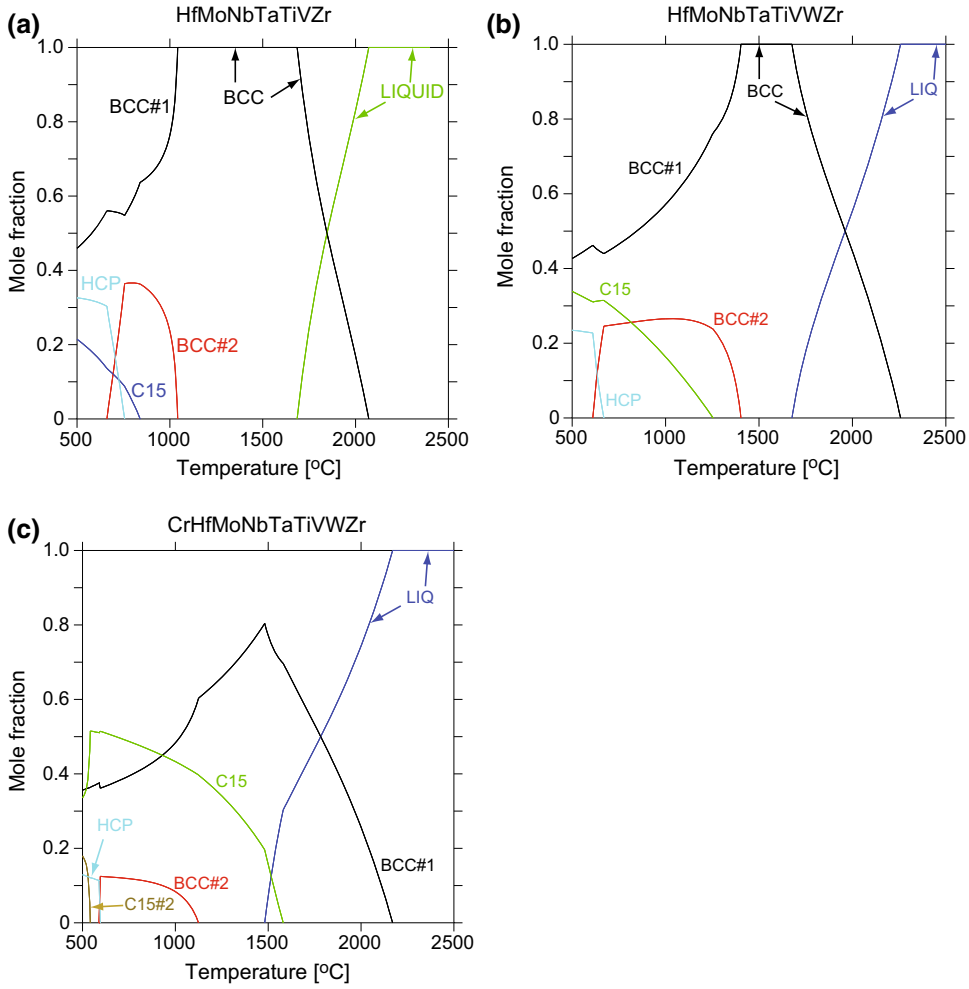

Fig. 5. Calculated equilibrium mole fraction for (a) HfMoNbTaTiVZr, (b) HfMoNbTaTiVWZr, and (c) CrHfMoNbTaTiVWZr.

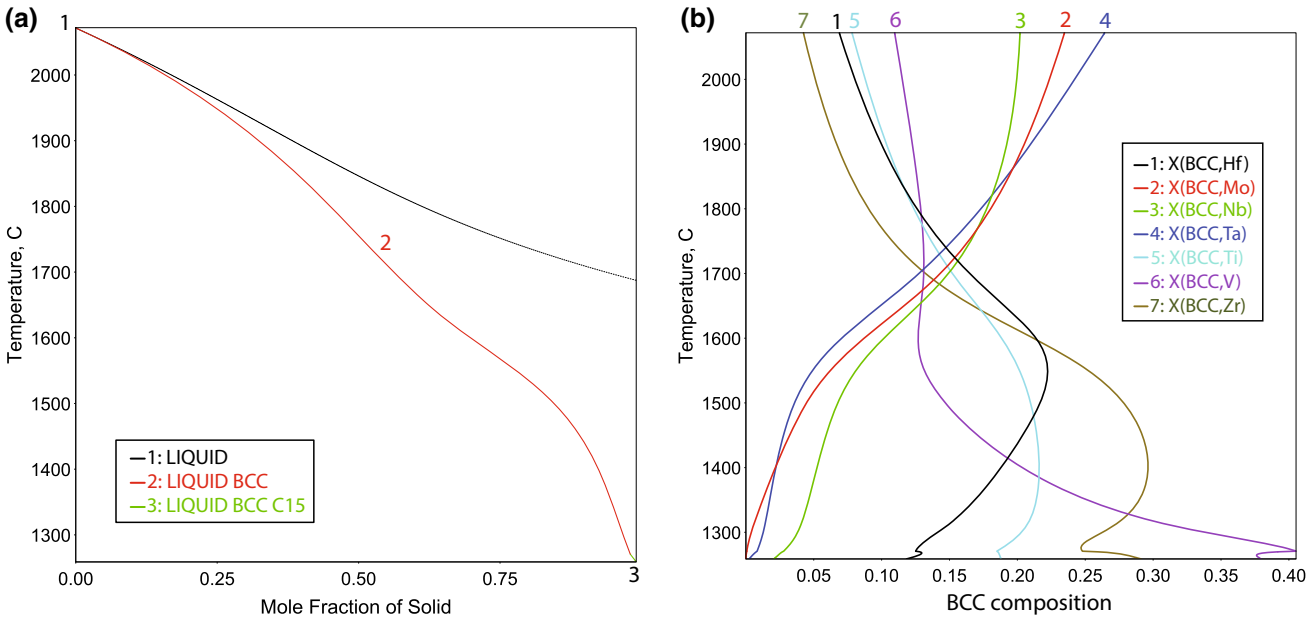

Fig. 6. Calculated (a) mole fraction of solids and (b) composition of bcc phase in HfMoNbTaTiVZr during nonequilibrium solidification using the Scheil–Gulliver models.

Table II. Measured compositions (at.%) of the bulk, the coarse dendrites (Denoted as "D Coarse"), and the coarse interdendritic regions (Denoted as "ID coarse"), and the fine dendrites (Denoted as "D Fine") in HfMoNbTaTiVZr and HfMoNbTaTiVWZr

		Hf	Mo	Nb	Ta	Ti	V	W	Zr
HfMoNbTaTiVZr	XRF	7.5	15.1	15.6	15.4	16.4	13.6		16.4
	D (coarse)	11 ± 1	19 ± 1	19 ± 1	21 ± 1	12 ± 1	11 ± 1		8.5 ± 1
	ID (coarse)	16 ± 1	11 ± 1	13 ± 1	7.6 ± 1	15 ± 1	15 ± 1		24 ± 1
	D (fine)	15 ± 1	13 ± 1	8.9 ± 1	5.3 ± 1	9.7 ± 1.5	23 ± 2		24 ± 2
HfMoNbTaTiVWZr	XRF	13.9	11.0	10.9	15.9	12.7	11.5	10.8	13.3
	D (coarse)	5.8 ± 1	15 ± 1	14 ± 1	21 ± 1	7.9 ± 1	8.6 ± 1	23 ± 1	4 ± 1.8
	ID (coarse)	16 ± 1	9.5 ± 1	12 ± 1	6.8 ± 1	13 ± 1	13 ± 1	4.9 ± 1	24 ± 1
	D (fine)	18 ± 1	8.8 ± 1.5	11 ± 1	1.2 ± 1	14 ± 2	15 ± 2	3.8 ± 1	28 ± 2

CALPHAD Calculations

The equilibrium mole fraction of phases versus temperature plots for quinary and senary alloys are shown in Figs. 3 and 4, respectively. The modeling predicts that the bcc phase is stable across a relatively wide temperature range for these eight alloys. At lower temperatures, the bcc phase decomposes into two bcc phases; one bcc phase is enriched in bcc elements and the other one is enriched in hcp elements, such as Hf, Ti, and Zr. For the septenary, octonary, and ennead alloys shown in Fig. 5, the bcc phase becomes more susceptible to decomposition with an increasing number of components, whereas the C15 phase becomes more stable. As a result, the bcc phase becomes less stable.

The mole fraction of solid phases as a function of temperature for the HfMoNbTaTiVZr alloy during nonequilibrium solidification (using the Scheil–Gulliver models)[23,24] is shown in Fig. 6. The simulation predicts formation of dominant bcc solid solution phase and a minor C15 phase that forms at the end of solidification. At the beginning of solidification, the bcc phase is enriched in Ta followed by Mo and Nb, whereas it is primarily depleted in Zr, followed by Hf, Ti, and V.

EXPERIMENTAL RESULTS

A single bcc solid-solution microstructure has been experimentally verified for several alloys listed in Table I, namely MoNbTaTiZr,[7] MoNbTaTiVW,[14] HfNbTaTiVZr,[15] and CrMoNbTaVW.[27] The present modeling work suggests that formation of a single bcc solid solution is possible in HfMoNbTaTiVZr but is unlikely in HfMoNbTaTiVWZr. To verify the model prediction, two alloys in the nominal molar compositions of HfMoNbTaTiVZr and HfMoNbTaTiVWZr with a total weight of ~200 g were fabricated using the arc-melting technique. The starting raw metallic elements have a purity of 99.0 wt.%. The bulk compositions of the as-cast alloys (Table II) were determined by x-ray fluorescence (XRF) using a Rigaku ZSX Primus II (Rigaku Corporation, Tokyo, Japan). X-ray diffraction (XRD) scans were done with an Ultima III (Rigaku Corporation) using Cu K-alpha radiation. Micrographs and elemental analysis of all samples were generated with an FEI Inspect F50 (FEI Company, Hillsboro, OR) scanning electron microscope [SEM-energy-dispersive spectroscopy (EDS)].

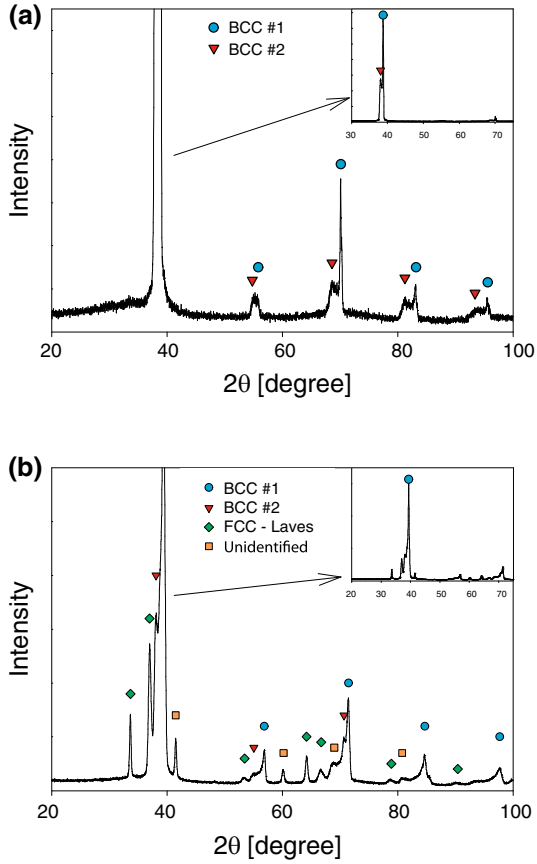

Fig. 7. XRD pattern of (a) HfMoNbTaTiVZr and (b) HfMoNbTaTiVWZr in the as-cast state.

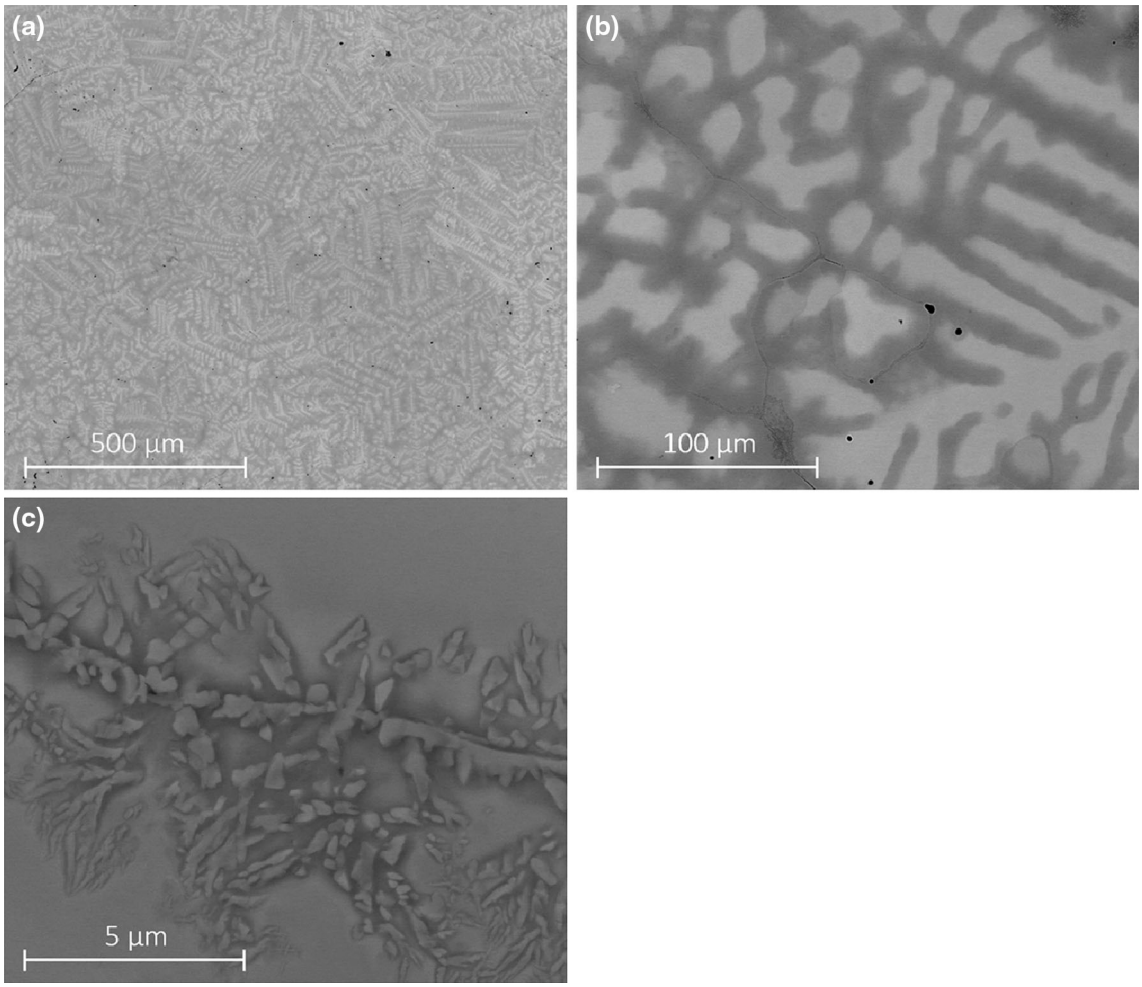

Fig. 8. SEM micrograph of the as-cast HfMoNbTaTiVZr: (a) overall image, (b) coarse dendrites, and (c) fine dendrites from the dark background.

Figure 7 compares the XRD patterns of the septenary and octonary alloys in the as-cast state. Two bcc phases are identifiable in HfMoNbTaTiVZr. The phase relation in HfMoNbTaTiVWZr is more complex; it contains two bcc phases, a C15 Laves phase, and an additional unidentified phase(s), which will require further study and more dedicated tools to identify, such as transmission electron microscopy (TEM).

A typical dendritic microstructure was observed in HfMoNbTaTiVZr in the as-cast state. This is shown in Fig. 8. The as-cast microstructure consists of a dominant set of coarse dendrites with a minor set of fine dendrites distributed in the dark background. The former forms during the primary crystallization, whereas the latter forms during the later stages of solidification. The elemental distributions within the grains (see Fig. 9) show that Ta, Mo, and Nb segregate to the "coarse" dendrites, whereas Hf, Ti, V, and Zr segregate to the "coarse" interdendritic regions. Quantitative chemical compositions from typical line scans are shown in Fig. 10, and the chemical compositions for the two sets of dendrites are listed in Table II. For the "coarse" dendrites, enrichment with Ta is observed whereas Zr shows the most depletion. Conversely, the "fine" dendrites are enriched in Zr and Hf but are depleted of Ti and Nb. The SEM–EDS elemental composition measurements qualitatively agrees with the Scheil–Gulliver simulation.

The as-cast microstructure of HfMoNbTaTiVWZr (see Fig. 11) is similar to HfMoNbTaTiVZr. Two sets of dendrites were observed. The coarse dendrites represent the primary crystalline phase with the bcc structure, whereas the fine set of dendrites forms at the later stages of crystallization. The elemental segregation (see Fig. 12) behavior is very similar to HfMoNbTaTiVZr, but W also segregates to these coarse dendrites because W has the highest melting point among the constituent elements. The

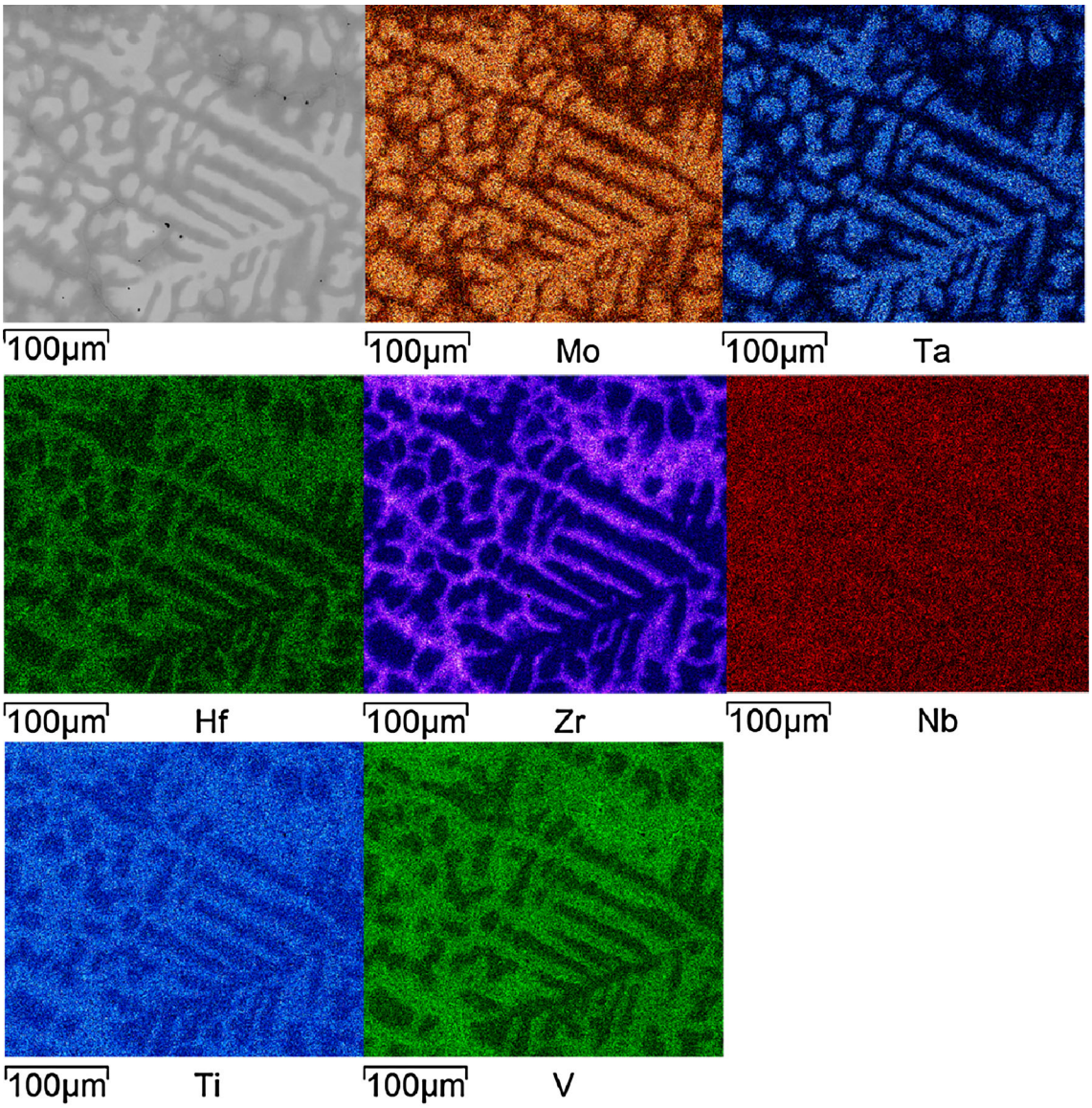

Fig. 9. SEM backscattered electron image and EDS mapping of Hf, Mo, Nb, Ta, Ti, V, and Zr in the as-cast HfMoNbTaTiVZr.

Rockwell hardness tests were done using 150 kgf load on four random areas, and the measured H_{RC} values are 48.6 ± 1.3 and 54.6 ± 0.5 for HfMoNbTaTiVZr and HfMoNbTaTiVWZr, respectively.

DISCUSSION

HEA Formation Rules

After surveying a large of number of alloys including solid-solution alloys, intermetallic compounds, and BMGs, Zhang et al.[6] originally proposed an empirical rule for forming HEAs; if a combination of $-15 \le \Delta H_{mix}^{liq} \le +5$ kJ/mol and $\delta \le 5\%$ is met, then disordered solid-solution phase is favored. An additional rule was proposed by Zhang et al.[8] that a combination of $\Omega \ge 1$ and $\delta \le 6.6\%$ also favors disordered solid-solution formation. Although these rules were proposed based on known experimental data, applying them for new alloys might not always work because they do not take into account the competing phases in the system.[11]

According to these rules,[8] all 16 alloys would favor forming disordered solid solution because the calculated empirical parameters are $-6.5 \le \Delta H_{mix}^{liq} \le +2.7$ kJ/mol, $\delta \le 6.07\%$, and $\Omega \ge 5.6$. Although the majority of the alloys probably will form single-phase HEAs (e.g., MoNbTaTiZr[7] and HfNbTaTiVZr[15]), exceptions were observed in HfMoNbTaTiVZr and HfMoNbTaTiVWZr. Two bcc phases were observed in the former and multiple phases formed in the latter. CALPHAD

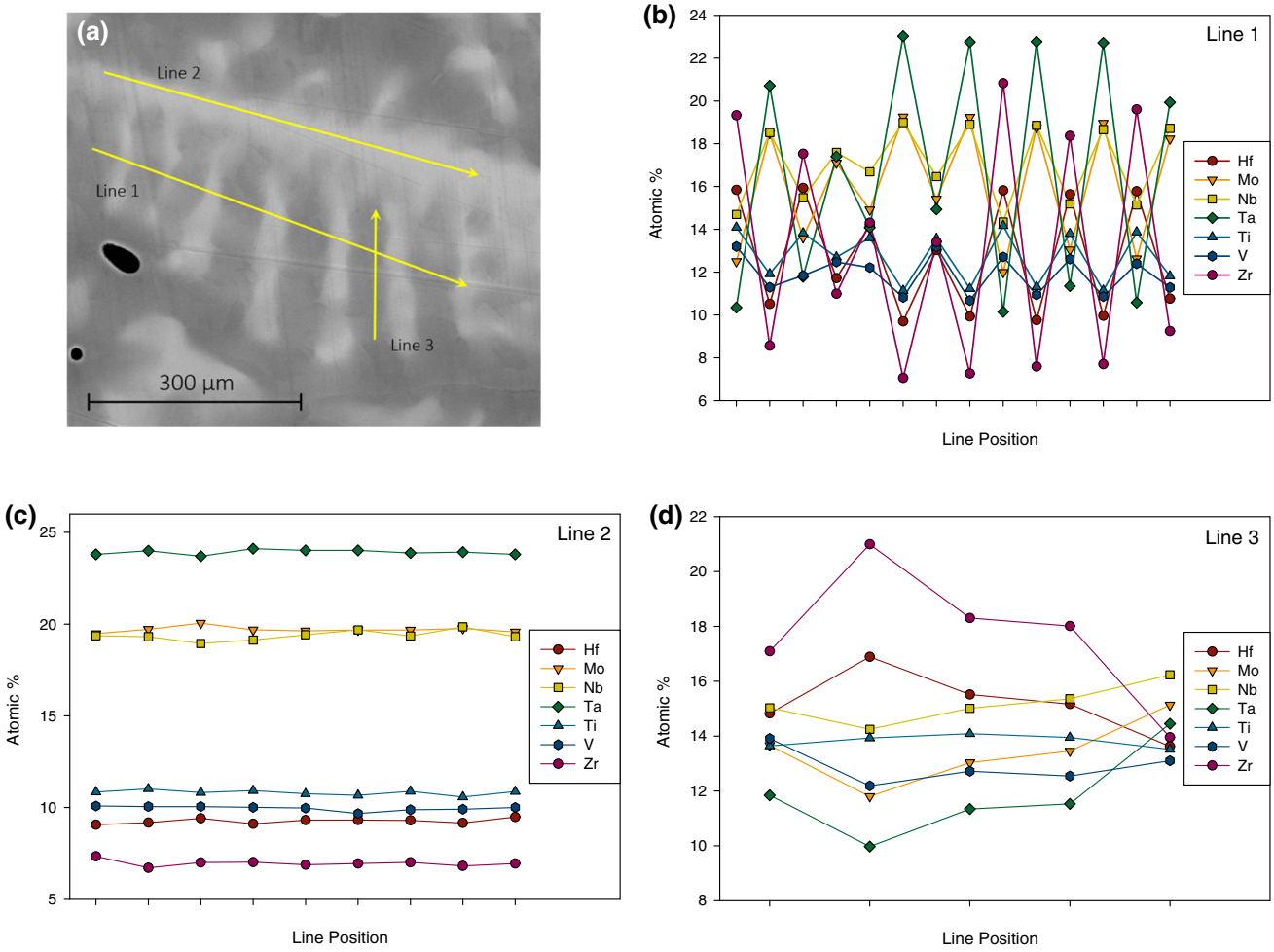

Fig. 10. (a) Backscattered electron micrograph of as-cast HfMoNbTaTiVZr. Composition profile (at.%) from EDS line scans: (b) across the dendrite-interdendrite regions, (c) along the dendrite, and (d) along the interdendrites.

also predicts formation of multiple phases in CrHfMoNbTaTiVWZr even though it has the highest entropy of mixing among the 16 alloys studied. In other words, entropy might not always dominate the phase stability as observed by Otto et al.[28] in CoCrFeMnNi-based HEAs because the competing phases and the enthalpy effect can overweigh the entropy effect.

On the other hand, these empirical parameters combine geometrical, physical, and thermodynamic properties of the alloy system of interest, so they should reflect, at least partially, some aspect of the free energy of the system. Because the phase diagrams are determined by the free energies of all phases in the system in the space of composition, temperature, and pressure, they are the key to understanding HEA formation from the thermodynamics point of view. In fact, as emphasized in Refs. [4,11–13], and [29], performing phase diagram calculations using CALPHAD has proven to be an effective searching tool. The efficient searching strategy proposed by Gao and Alman[11] has been used to design a variety of new single-phase HEAs in hcp,[16,30] fcc,[30] and bcc[30] structures. It should be emphasized that the reliability of CALPHAD prediction is critically grounded in the reliability of the underlying thermodynamic database assessment. As pointed out by Zhang and Gao,[29] assessment for all constituent binaries and ternaries in the database is usually required for the best and most accurate prediction results.

An open question remaining in the HEA community centers on whether there is a limit on the total number of principal components in a solid-solution phase. The current study attempts to answer this question for the bcc structure. A previous study by Gao et al. attempted to predict single-hcp HEAs using phase diagram inspection, CALPHAD modeling, and AIMD simulations.[16] They suggested the possibility in forming decadal single-hcp HEAs

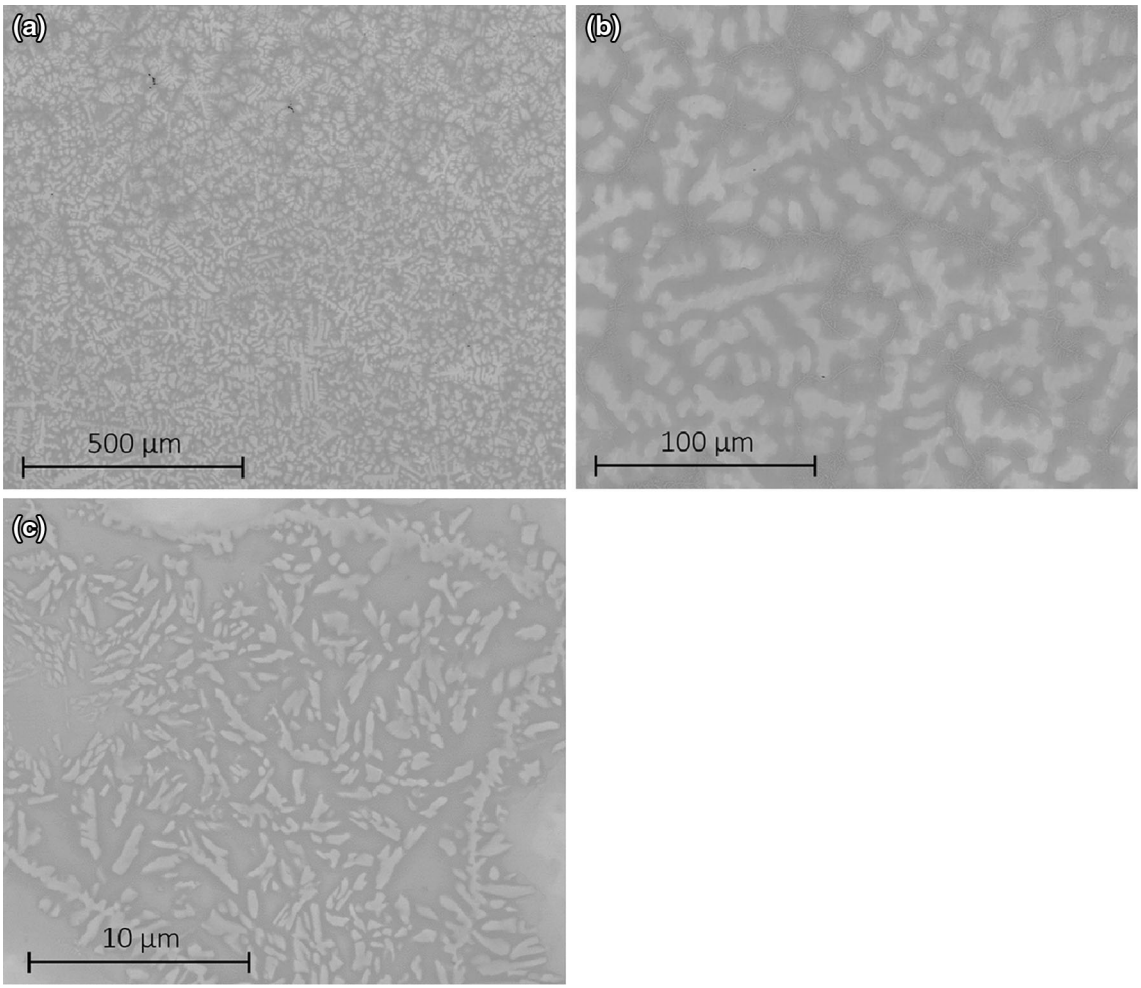

Fig. 11. SEM micrograph of the as-cast HfMoNbTaTiVWZr: (a) overall microstructure at low magnification, (b) coarse dendrites, and (c) fine dendrites in the dark background.

based on rare-earth elements. BCC phase was observed in HfNbTaTiZr,[26] but the formation of senary bcc HEAs had not been widely studied. Several compositions suggested in Table I hold the possibility of verifying this. As a matter of fact, MoNbTaTiVW,[14] HfNbTaTiVZr,[15] and CrMoNbTaVW[27] have been experimentally confirmed. However, single bcc solid solution was not observed in either HfMoNbTaTiVZr or HfMoNbTaTiVWZr. Also, multiple phases are predicted to form in CrHfMoNbTaTiVWZr. As a result, searching for single-bcc HEAs with more than seven principal elements may need further consideration for non-refractory elements such as Re. Rhenium is known to have large solubility in refractory bcc alloys according to binary phase diagrams.[31]

Nonetheless, composites based on the high-entropy concept should not be ignored because the total entropy can still be significantly higher than traditional alloys as reported by Santodonato et al.[32] in $Al_{1.3}$CoCrCuFeNi. In addition, a well-designed composite microstructure may provide combined strength and ductility that could be important for structural materials applications. Miracle et al.[33] proposed a strategy to design particle-strengthened HEAs for structural applications in the transportation and energy sectors.

HfNbTaTiZr-M (M = Cr, Mo, V, and W) Pseudo-Binary Phase Diagrams

As an example to demonstrate application of CALPHAD in HEA design, phase diagrams and thermodynamic analyses are performed on the HfNbTaTiZr-M (M = Cr, Mo, V, and W) pseudo-binary systems. An objective of the study was to identify additional principal refractory elements that promote formation of a single bcc solid solution based on HfNbTaTiZr.[26] The HfNbTaTiZr-M pseudo-binary phase diagrams were predicted using

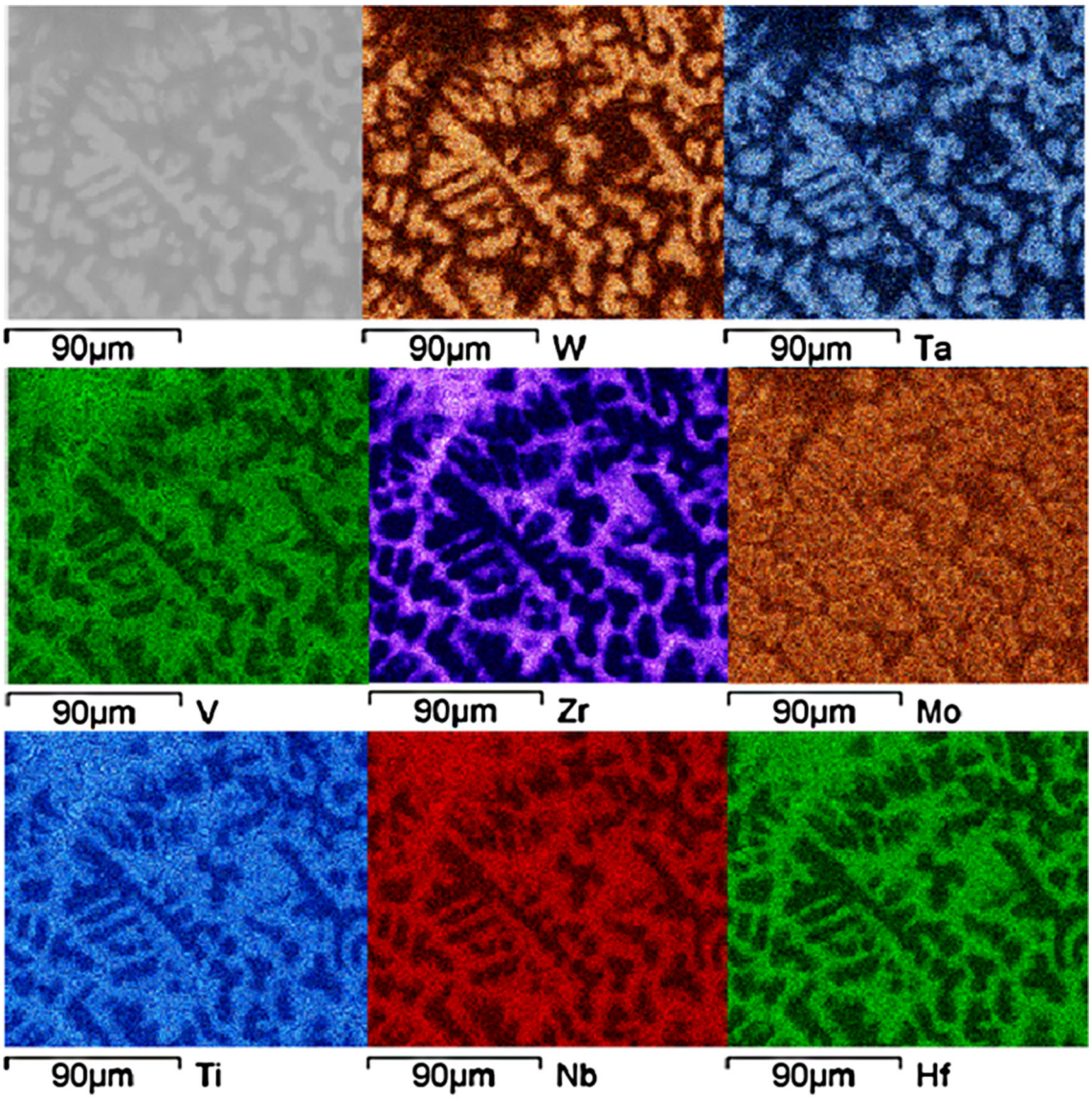

Fig. 12. SEM backscattered electron image and EDS mapping of Hf, Mo, Nb, Ta, Ti, V, W, and Zr in the as-cast HfMoNbTaTiVWZr.

the TCNI7 database as shown in Fig. 13. Clearly, the addition of Mo causes formation of an isomorphous bcc phase at high temperatures. The V solubility in the bcc phase is limited to 52 at.% at 1383°C, whereas Cr and W solubilities are very small.

Figure 14a shows entropy of mixing for the bcc phase (namely, $\Delta S_{\text{mix}}^{\text{bcc}}$, $\Delta H_{\text{mix}}^{\text{bcc}}$, and $\Delta G_{\text{mix}}^{\text{bcc}}$) in HfNbTaTiZr-M (M = Cr, Mo, V, and W) pseudo-binaries at 1000°C. HfNbTaTiZr-Cr shows positive excess entropy, whereas HfNbTaTiZr-Mo and HfNbTaTiZr-W show negative excess entropy. The $\Delta S_{\text{mix}}^{\text{bcc}}$ value for HfNbTaTiZr-Mo is fairly close to the ideal mixing. It was seen that deviation from ideal mixing for all systems was not large. In sharp contrast to the $\Delta S_{\text{mix}}^{\text{bcc}}$ value, the $\Delta H_{\text{mix}}^{\text{bcc}}$ value shows significant variation with respect to alloying elements (see Fig. 14b). With the addition of Cr, $\Delta H_{\text{mix}}^{\text{bcc}}$ increases much more than with V additions. The addition of Mo, on the other hand, lowers $\Delta H_{\text{mix}}^{\text{bcc}}$ much more than W does. The biggest difference in $\Delta H_{\text{mix}}^{\text{bcc}}$ between systems occurs within approximately 50–70 at.% for M. The trend in $\Delta G_{\text{mix}}^{\text{bcc}}$ (see Fig. 14c) follows $\Delta H_{\text{mix}}^{\text{bcc}}$, indicating that the enthalpy of mixing outweighs the entropy of mixing in these systems.

Figure 15a–c shows the values of $\Delta S_{\text{mix}}^{\text{C15}}$, $\Delta H_{\text{mix}}^{\text{C15}}$, and $\Delta G_{\text{mix}}^{\text{C15}}$ as a function of M contents for the C15 phase in these HfNbTaTiZr-M pseudo-binaries. The

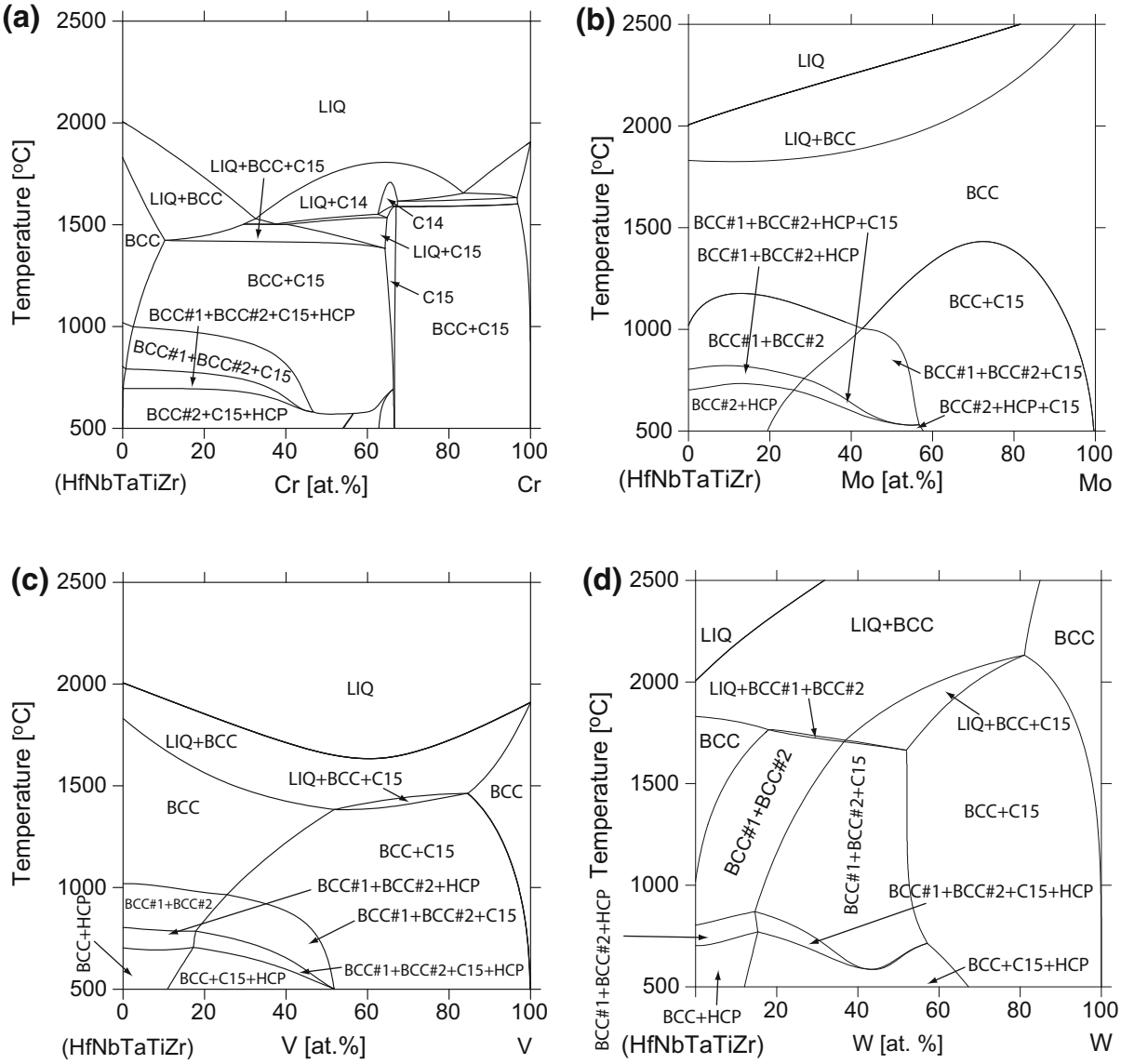

Fig. 13. Calculated isopleth of (a) HfNbTaTiZr-Cr, (b) HfNbTaTiZr-Mo, (c) HfNbTaTiZr-V, and (d) HfNbTaTiZr-W pseudo-binaries.

addition of W lowers $\Delta S_{\text{mix}}^{\text{C15}}$to a minimum value of −6.1 J/K/mol, thereby suggesting that strong ordering might take place in C15 phase. In contrast, the impact on $\Delta S_{\text{mix}}^{\text{C15}}$ due to addition of Cr, Mo, or V is much smaller. The $\Delta H_{\text{mix}}^{\text{C15}}$ values all reach a minimum at 40–70 at.% M, with descending order given as: V > Mo > Cr > W. After combining entropy and enthalpy effects, the minimum value of $\Delta G_{\text{mix}}^{\text{C15}}$ in descending order is: V > Mo > W > Cr.

Although computational modeling was performed on only 16 alloys (see Table I) in this study, the same methodologies (i.e., comparing the predictions from empirical parameters and CALPHAD modeling with experiments) can be applied to other compositions. Accumulating computational and experimental data will help refine existing rules and discover new rules pertaining to solid-solution HEA formation.

CONCLUSION

Analyses on formation of disordered bcc solid solution in 16 alloys were performed in this study using both the empirical parameters [including atomic size difference (δ),[6] enthalpy of mixing (ΔH_{mix}),[6] electronegativity difference ($\Delta\chi$),[9] and the Ω-parameter[8]] and CALPHAD approach. Experimental verification on HfMoNbTaTiVZr and HfMoNbTaTiVWZr using XRD, EDS, and SEM demonstrated the effectiveness of CALPHAD approach over empirical parameters. New single bcc HEAs were suggested. The following conclusions were reached:

1. Although aforementioned empirical parameters are useful in HEA design, they are not conclusive because they do not take into account competing phases.

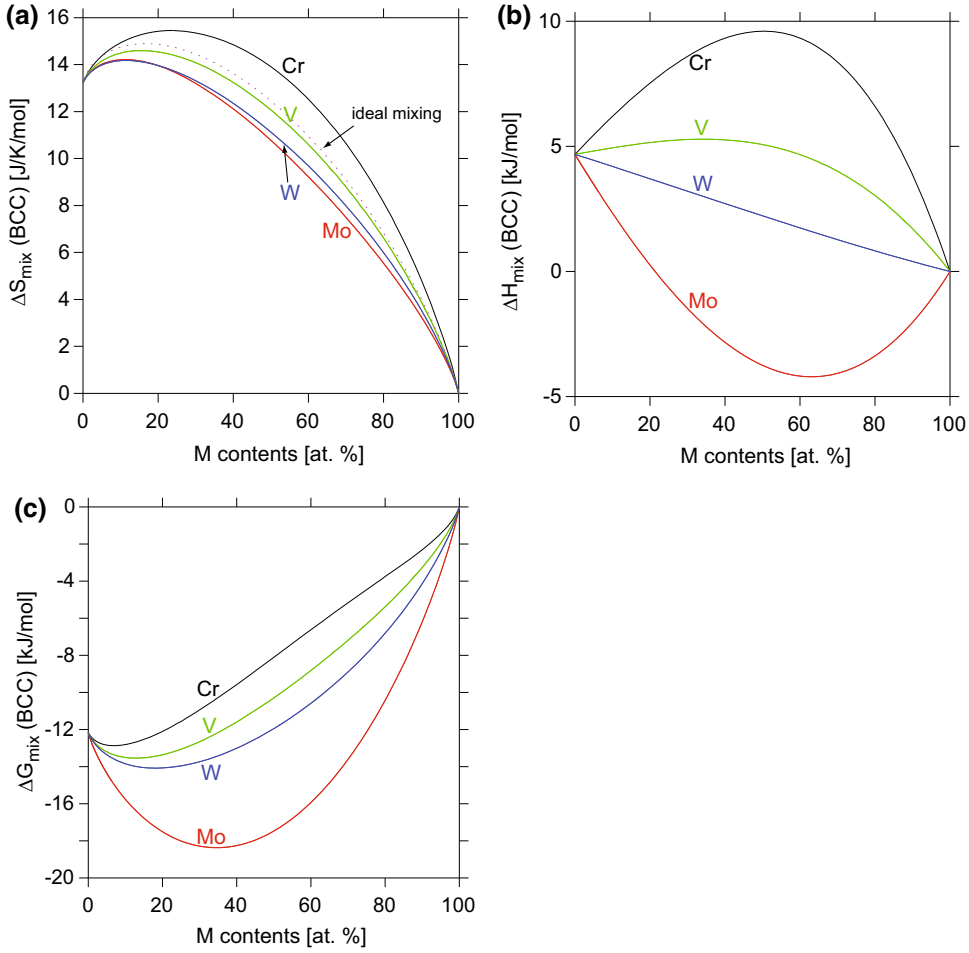

Fig. 14. Calculated (a) entropy of mixing, (b) enthalpy of mixing, and (c) Gibbs energy of mixing for the bcc phase at 1000°C in HfNbTaTiZr-M (M = Cr, Mo, V, W) pseudo-binaries.

2. The calculated entropies of mixing for both liquid and bcc phases are very close to the value of ideal mixing.
3. Good agreement in the enthalpy of mixing for the liquid phase was observed using the Takeuchi table via Eq. 1 and using CALPHAD. They are all negative except NbTaTiVZr, HfNbTaTiVZr, and HfNbTaTiZr.
4. The enthalpy of mixing for the bcc phase contrasts that for the liquid phase noticeably for most alloys. The former is negative for alloys that consist of only bcc metals, and it becomes positive when mixing bcc metals with hcp metals.
5. The CALPHAD method with reliable thermodynamic database has been shown to be an efficient tool when searching for new single-phase HEAs. New single-bcc-phase HEAs are suggested: HfMoNbTiZr, HfMoTaTiZr, NbTaTiVZr, HfMoNbTaTiZr, HfMoTaTiVZr, and MoNbTaTiVZr.
6. Two bcc phases formed in the as-cast HfMoNbTaTiVZr. It was observed that the coarse dendritic regions were primarily enriched in Ta, followed by Mo and Nb; the coarse interdendritic regions, on the other hand, were enriched in Hf, Ti, V, and Zr. The observed microsegregation behavior qualitatively agrees with the prediction from Scheil–Gulliver models.
7. Multiple phases formed in the as-cast HfMoNbTaTiVWZr. It was observed that the coarse dendrites were enriched in W, in this case, followed by Ta, Mo, and Nb. The coarse interdendritic regions were again enriched in Hf, Ti, V, and Zr.
8. For the HfNbTaTiZr-M pseudo-binaries at 1000°C, the bcc phase field, in descending order, was found to be: Mo $\gg$ V $\gg$ W $>$ Cr. Molybdenum additions lowered $\Delta H_{\text{mix}}^{\text{bcc}}$ the most (and accordingly $\Delta G_{\text{mix}}^{\text{bcc}}$). In contrast Cr additions increased $\Delta H_{\text{mix}}^{\text{bcc}}$ the most (and thus,$\Delta G_{\text{mix}}^{\text{bcc}}$).
9. For the HfNbTaTiZr-M pseudo-binaries at 1000°C, W additions lowered $\Delta H_{\text{mix}}^{\text{C15}}$ substantially and caused $\Delta S_{\text{mix}}^{\text{C15}}$ to decrease. The minimum value of $\Delta G_{\text{mix}}^{\text{C15}}$ in descending order was: V $>$ Mo $>$ W $>$ Cr.

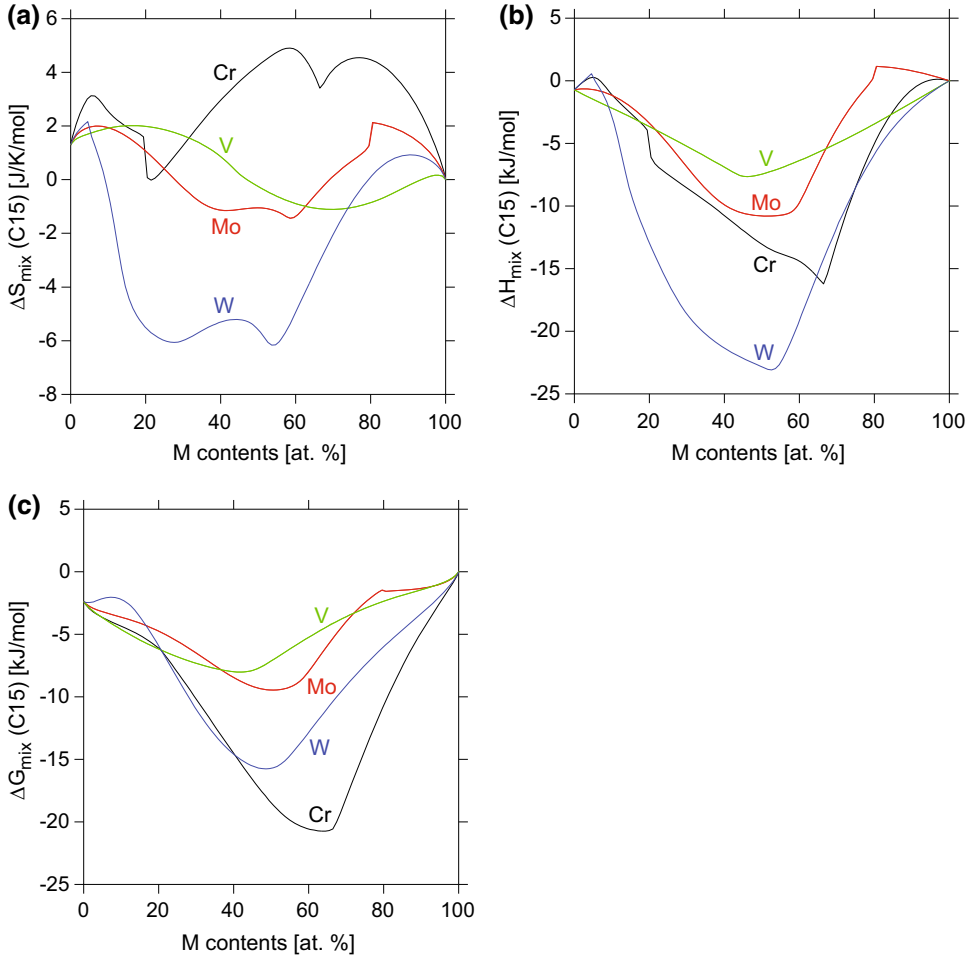

Fig. 15. Calculated (a) entropy of mixing, (b) enthalpy of mixing, and (c) Gibbs energy of mixing for the C15 phase in HfNbTaTiZr-M (M = Cr, Mo, V, W) pseudo-binaries at 1000°C.

ACKNOWLEDGEMENTS

This work was funded by the Cross-Cutting Technologies Program at the National Energy Technology Laboratory (NETL)—Strategic Center for Coal, managed by Robert Romanosky (Technology Manager) and Charles Miller (Technology Monitor). The Research was executed through NETL's Office of Research and Development's Innovative Process Technologies (IPT) Field Work Proposal. Research performed by AECOM Staff was conducted under the RES contract DE-FE-0004000. The authors thank Ed Argetsinger (AECOM) for making the ingots, Paul Danielson (NETL) for performing optical microscopy, Chris Powell (AECOM) for performing hardness tests, Richard Chin (NETL) for performing WDXRF analysis, and Kyle Rozman (NETL/ORISE) performing x-ray diffraction. M.C.G. thanks from Andreas Markström, Huahai Mao, and Chao Jiang from Thermo-Calc for providing technical support.

DISCLAIMER

This project was funded by the Department of Energy, National Energy Technology Laboratory, an agency of the United States Government, through a support contract with AECOM. Neither the United States Government nor any agency thereof, nor any of their employees, nor AECOM, nor any of their employees, makes any warranty, expressed or implied, or assumes any legal liability or responsibility for the accuracy, completeness, or usefulness of any information, apparatus, product, or process disclosed, or represents that its use would not infringe privately owned rights. Reference herein to any specific commercial product, process, or service by trade name, trademark, manufacturer, or otherwise, does not necessarily constitute or imply its endorsement, recommendation, or favoring by the United States Government or any agency thereof. The views and opinions of authors expressed herein

do not necessarily state or reflect those of the United States Government or any agency thereof.

REFERENCES

1. J.W. Yeh, S.K. Chen, S.J. Lin, J.Y. Gan, T.S. Chin, T.T. Shun, C.H. Tsau, and S.Y. Chang, *Adv. Eng. Mater.* 6, 299 (2004).
2. B. Cantor, I.T.H. Chang, P. Knight, and A.J.B. Vincent, *Mater. Sci. Eng. A* 375–377, 213 (2004).
3. J.W. Yeh, *JOM* 65, 1759 (2013).
4. Y. Zhang, T.T. Zuo, Z. Tang, M.C. Gao, K.A. Dahmen, P.K. Liaw, and Z.P. Lu, *Prog. Mater. Sci.* 61, 1 (2014).
5. M.C. Gao, J.W. Yeh, P.K. Liaw, and Y. Zhang, *High-Entropy Alloys: Fundamentals and Applications* (Cham: Springer, 2015).
6. Y. Zhang, Y.J. Zhou, J.P. Lin, G.L. Chen, and P.K. Liaw, *Adv. Eng. Mater.* 10, 534 (2008).
7. Y. Zhang, X. Yang, and P.K. Liaw, *JOM* 64, 830 (2012).
8. Y. Zhang, Z.P. Lu, S.G. Ma, P.K. Liaw, Z. Tang, Y.Q. Cheng, and M.C. Gao, *MRS Commun.* 4, 57 (2014).
9. M.G. Poletti and L. Battezzati, *Acta Mater.* 75, 297 (2014).
10. S. Guo, C. Ng, J. Lu, and C.T. Liu, *J. Appl. Phys.* 109, 103505 (2011).
11. M.C. Gao and D.E. Alman, *Entropy* 15, 4504 (2013).
12. C. Zhang, F. Zhang, S.L. Chen, and W.S. Cao, *JOM* 64, 839 (2012).
13. F. Zhang, C. Zhang, S.L. Chen, J. Zhu, W.S. Cao, and U.R. Kattner, *CALPHAD* 45, 1 (2014).
14. B. Zhang, M.C. Gao, Y. Zhang, S. Yang, and S.M. Guo, *Mater. Sci. Technol.* 31, 1207 (2015).
15. M.C. Gao, B. Zhang, S. Yang, and S.M. Guo, *Metall. Mater. Trans. A* (2015). doi:10.1007/s11661-015-3105-z.
16. M.C. Gao, B. Zhang, S.M. Guo, J.W. Qiao, and J.A. Hawk, *Metall. Mater. Trans. A* (2015). doi:10.1007/s11661-015-3091-1.
17. O.N. Senkov, J.D. Miller, D.B. Miracle, and C. Woodward, *Nature Commun.* 6, 6529 (2015).
18. M.C. Troparevsky, J.R. Morris, P.R.C. Kent, A.R. Lupini, and G.M. Stocks, *Phys. Rev. X* 5, 011041 (2015).
19. A. Takeuchi and A. Inoue, *Mater. Trans. JIM* 46, 2817 (2005).
20. A.R. Miedema, F.R. de Boer, and R. Boom, *CALPHAD* 1, 341 (1977).
21. S. Fang, X. Xiao, L. Xia, W. Li, and Y. Dong, *J. Non-Cryst. Solids Solids* 321, 120 (2003).
22. B. Sundman, B. Jansson, and J.O. Andersson, *CALPHAD* 9, 153 (1985).
23. G.H. Gulliver, *J. Inst. Metals* 9, 120 (1913).
24. E. Scheil, *Z. Metallkd.* 34, 70 (1942).
25. O.N. Senkov, G.B. Wilks, D.B. Miracle, C.P. Chuang, and P.K. Liaw, *Intermetallics* 18, 1758 (2010).
26. O.N. Senkov, J.M. Scott, S.V. Senkova, D.B. Miracle, and C.F. Woodward, *J. Alloys Compd.* 509, 6043 (2011).
27. B. Zhang, M.C. Gao, Y. Zhang, and S.M. Guo, *CALPHAD* (under review, 2015).
28. F. Otto, Y. Yang, H. Bei, and E.P. George, *Acta Mater.* 61, 2628 (2013).
29. C. Zhang and M.C. Gao, *High-Entropy Alloys: Fundamentals and Applications, ch.12*, ed. M.C. Gao, J.W. Yeh, P.K. Liaw, and Y. Zhang (Cham: Springer, 2015).
30. M.C. Gao, *High-Entropy Alloys: Fundamentals and Applications, ch. 11*, ed. M.C. Gao, J.W. Yeh, P.K. Liaw, and Y. Zhang (Cham: Springer, 2015).
31. ASM Alloy Phase Diagram Database, http://www1.asminternational.org/asmenterprise/apd/.
32. L.J. Santodonato, Y. Zhang, M. Feygenson, C.M. Parish, M.C. Gao, R.J.K. Weber, J.C. Neuefeind, Z. Tang, and P.K. Liaw, *Nature Commun.* 6, 5964 (2015).
33. D.B. Miracle, J.D. Miller, O.N. Senkov, C. Woodward, M.D. Uchic, and J. Tiley, *Entropy* 16, 494 (2014).